This is the accepted version of the following article:

Li J., Xu X., Luo Z., Zhang C., Yu X., Zuo Y., Zhang T., Tang P., Arbiol J., Llorca J., Liu J., Cabot A.. Compositionally tuned Ni x Sn alloys as anode materials for lithium-ion and sodium-ion batteries with a high pseudocapacitive contribution. Electrochimica Acta, (2019). 304. : 246 - . 10.1016/j.electacta.2019.02.098,

which has been published in final form at https://dx.doi.org/10.1016/j.electacta.2019.02.098 © https://dx.doi.org/10.1016/j.electacta.2019.02.098. This manuscript version is made available under the CC-BY-NC-ND 4.0 license
http://creativecommons.org/licenses/by-nc-nd/4.0/

Compositionally tuned Ni_xSn alloys as anode materials for lithium-ion and sodium-ion batteries with a high pseudocapacitive contribution

Junshan Li,[a,b,○] Xijun Xu,[c,d,○] Zhishan Luo,[a] Chaoqi Zhang,[a] Xiaoting Yu,[a] Yong Zuo,[a] Ting Zhang,[e] Pengyi Tang,[e] Jordi Arbiol,[e,f] Jordi Llorca,[g] Jun Liu,[c,d,*] Andreu Cabot[a,f,*]

a Catalonia Institute for Energy Research - IREC, Sant Adrià de Besòs, Barcelona, 08930, Spain

b Departament d'Electronica, Universitat de Barcelona, 08028 Barcelona, Spain

c Guangdong Provincial Key Laboratory of Advanced Energy Storage Materials, School of Materials Science and Engineering, South China University of Technology, Guangzhou 510641, P. R. China

d SUNWODA-SCUT Joint Laboratory for Advanced Energy Storage Technology, South China University of Technology, Guangzhou 510641, P. R. China

e Catalan Institute of Nanoscience and Nanotechnology (ICN2), CSIC and BIST, Campus UAB, Bellaterra, 08193 Barcelona, Spain

f ICREA, Pg. Lluís Companys 23, 08010 Barcelona, Spain

g Institute of Energy Technologies, Department of Chemical Engineering and Barcelona Research Center in Multiscale Science and Engineering. Universitat Politècnica de Catalunya, EEBE, 08019 Barcelona, Spain

ABSTRACT

Nickel tin alloy nanoparticles (NPs) with tuned composition Ni_xSn ($0.6 \leq x \leq 1.9$) were synthesized by a solution-based procedure and used as anode materials for Li-ion batteries (LIBs) and Na-ion batteries (SIBs). Among the compositions tested, $Ni_{0.9}Sn$-based electrodes exhibited the best performance in both LIBs and SIBs. As LIB anodes, $Ni_{0.9}Sn$-based electrodes delivered charge-discharge capacities of 980 mAh g^{-1} after 340 cycles at 0.2 A g^{-1} rate, which surpassed their maximum theoretical capacity considering that only Sn is lithiated. A kinetic characterization of the charge-discharge process demonstrated the electrode performance to be aided by a significant pseudocapacitive contribution that compensated for the loss of energy storage capacity associated to the solid-electrolyte interphase formation. This significant pseudocapacitive contribution, which not only translated into higher capacities but also longer durability, was associated to the small size of the crystal domains and the proper electrode composition. The performance of Ni_xSn-based electrodes toward Na-ion storage was also characterized, reaching significant capacities above 200 mAh g^{-1} at 0.1 A g^{-1} but with a relatively fast fade over 120 continuous cycles. A relatively larger pseudocapacitive contribution was obtained in Ni_xSn-based electrodes for SIBs when compared with LIBs, consistently with the lower contribution of the Na ion diffusion associated to its larger size.

Keywords: colloidal bimetallic nanoparticles; nickel tin alloy; anode materials; lithium-ion batteries; sodium-ion batteries.

INTRODUCTION

Lithium ion batteries (LIBs) have become essential in portable electronic applications. However, while widely spread in the market, current LIBs are far from being optimized electrochemical energy storage devices.[1–5] LIBs still suffer from moderate durabilities and current densities, which are in large part associated to the limitations of actual electrode materials. Additionally, the availability of lithium poses middle-long term limitations to this technology.[6,7] Thus, the development of improved electrode materials for LIBs and alternative battery technologies based on more abundant ions, such as sodium, is a worthwhile endeavor.

Current commercial LIBs use graphite as anode material, what limits the theoretic maximum energy density to 375 mAh g^{-1}.[8–11] On the other hand, sodium ion batteries (SIBs) cannot make use of graphite due to the insignificant Na-insertion in this material.[12–14] As an alternative anode material for both LIBs and SIBs, Sn and Sn-based alloys have been extensively studied due to their abundance, low toxicity and high energy density, 992 mAh g^{-1} for LIBs and 847 mAh g^{-1} for SIBs, corresponding to the formation of $Li_{22}Sn_5$ and $Na_{15}Sn_4$, respectively.[15–18] However, Sn undergoes huge volume changes during charge-discharge cycles that shorten its usage time.[19–24] This drawback can be partially overcome by reducing the size of the crystal domains in the electrode. The use of nanostructured electrodes provides additional advantages in terms of increasing rate capability, because of the shorter Li-ion diffusion paths, and increasing the pseudocapacitive contribution associated with the larger surface/volume ratios.[25–30] An additional strategy to improve stability is to alloy tin with non-active elements, reducing in this way the volume changes and potentially increasing the pseudocapacitive contribution. In this direction, bimetallic Sn-based allows such as Cu-Sn,[31–33] FeSn,[33–35] Co-Sn,[34–53] and Ni-Sn[17,33,54–56] have been tested as base materials for LIB and/or SIB electrodes with excellent results.

Not considering pseudocapacitive effects, the main drawback of alloying Sn with non-active metals is the decrease of the maximum energy density potentially achieved with the amount on non-active metal introduced. Thus, the alloy composition needs to be finely and continuously tuned along the whole solid-solution range to find the optimal composition. However, most previous works have focused on studding the performance of intermetallic Sn-based alloys, with strongly constrained compositions. In the present work, we take advantage of the versatility of colloidal synthesis method to produce nanoparticles (NPs) of a range of Ni-Sn solid solutions with Ni:Sn ratios from 0.6 to 1.9. After removing surface ligands, we use these NPs to test the performance Ni-Sn solid solutions as anode materials for LIBs and SIBs.

EXPERIMENTAL

Chemicals: Nickel(II) acetylacetonate ($Ni(acac)_2 \cdot xH_2O$ (x~2), 95%, Sigma-Aldrich), tin(II) acetate ($Sn(oac)_2$, 95%, Fluka), oleic acid (OAc, Sigma-Aldrich), oleylamine (OAm, 80-90%, TCI), tri-*n*-octylphosphine (TOP, 97%, Strem), borane tert-butylamine complex (TBAB, 97%, Sigma-Aldrich), TIMCAL Graphite & Carbon Super P (Super P, KJ group), polyvinylidene fluoride (PVDF, KJ group), N-methy1-2-pyrrolidone (NMP, 99%, Aladdin), hydrazine monohydrate (N_2H_4 64-65%, reagent grade, 98%, Sigma-Aldrich) and acetonitrile (CH_3CN, extra dry, Fisher) were used as received without any further purification. Chloroform, acetone and ethanol were of analytical grade and purchased from various sources. An argon-filled glove-box was used for storing and dealing with sensitive chemicals.

Colloidal Synthesis of NiSn NPs: All the syntheses were carried out using standard airless techniques using a vacuum/dry argon gas Schlenk line. Ni-Sn NPs were prepared following the scaled-up version of a protocol we previously detailed.[57] Briefly, 20 mL OAm, 1.0 mL OAc, 0.9 mmol $Ni(acac)_2 \cdot xH_2O$ and 0.6 mmol $Sn(oac)_2$ were loaded into a 50 mL three-neck flask containing a magnetic stirring bar. The reaction was strongly stirred and degassed under vacuum at 80 °C for 2 hours to remove water, air, and low-boiling point impurities. Then, a gentle flow of argon was introduced, 5 mL of TOP were injected and the reaction flask was heated to 180 °C at 5 °C/min. Meanwhile, a reducing solution was prepared by dissolving 5 mmol TBAB in 5 mL OAm through sonication for 30 min, and subsequently degassed this mixture for 1 hour at ambient temperature. This reducing solution was injected into the reaction flask containing the Ni and Sn precursor at 180 °C. Upon injection, a visible color change, from deep green to black, was immediately observed. The reaction was maintained at 180 °C for 1 hour, followed by a rapid cool down to room temperature using a water bath. The content of the reaction mixture was transferred to two centrifuge tubes, followed by centrifuging at 9000 rpm for 3 min after introducing acetone as non-solvent. The precipitate was suspended in chloroform and centrifuged again after adding additional acetone. This process was repeated twice. Finally, the NPs were suspended in 10 mL chloroform.

Ligand removal: The native organic ligands were removed from the NP surface according to a previously published report.[28,58] Briefly, 25 mL acetonitrile and 0.8 mL hydrazine hydrate was introduced into a vial containing the precipitated NPs. The mixture was stirred for 4 hours at room temperature and then collected by centrifuging at low speed. The product was further washed with acetonitrile and centrifuged at 2000 rpm for another 3 times. NPs were collected and stored in inert air atmosphere after drying under vacuum at room temperature.

Characterization: Powder x-ray diffraction (XRD) was measured on a Bruker AXS D8 Advance x-ray diffractometer with Cu K radiation (λ = 1.5106 Å) operating at 40 kV and 40 mA. Scanning electron microscopy (SEM) analyses were performed on a ZEISS Auriga SEM with an energy

dispersive X-ray spectroscopy (EDS) detector at 20 kV. Transmission electron microscopy (TEM) analyses were carried out on a ZEISS LIBRA 120, operating at 120 kV, using a 200 mesh Carbon-coated grid from Ted-Pella as substrate. High-resolution TEM (HRTEM) and scanning TEM (STEM) studies were carried out using a field emission gun FEI Tecnai F20 microscope at 200 kV with a point-to-point resolution of 0.19 nm. High angle annular dark-field (HAADF) STEM was combined with electron energy loss spectroscopy (EELS) in the Tecnai microscope by using a GATAN QUANTUM filter. For the ICP, 5 mg sample dessolved in 10 ml freshly prepared Agua Regia. 0.5 ml were taken into 24.5 ml MilliQ water. X-ray photoelectron spectroscopy (XPS) was done on a SPECS system equipped with an Al anode XR50 source operating at 150 mW and a Phoibos 150 MCD-9 detector. The pressure in the analysis chamber was kept below 10^{-7} Pa. The area analyzed was about 2 mm x 2 mm. The pass energy of the hemispherical analyzer was set at 25 eV and the energy step was maintained at 1.0 eV. Data processing was performed with the Casa XPS program (Casa Software Ltd., UK). Binding energies were shifted according to the reference C 1s peak that was located at 284.8 eV. The Fourier transform infrared spectrometer (FTIR) data were recorded on an Alpha Bruker spectrometer.

Electrochemical measurements: Ni-Sn NPs (80 wt%) were mixed with Super P (10 wt%), PVDF (10 wt%) and NMP. The obtained slurry was bladed onto a copper foil and dried at 80 ºC for 24 h in a vacuum oven. Working electrodes were obtained by cutting the printed foil into circular disk with a diameter of 12.0 mm. The mass loading of active materials was estimated to be 0.7-1.2 mg cm^{-2}. To test the performance of electrodes based on Ni-Sn NPs, half cells were assembled in the glove box (H_2O and O_2 < 0.1 ppm) using Celgard2400 as separator. As electrolyte for LIBs, a 1 M $LiPF_6$ solution in ethylene carbonate (EC)/diethyl carbonate (DEC) (1:1 in volume) with 5 vol% fluoroethylene carbonate (FEC) as additive was used. For SIBs, 1 M $NaClO_4$ in propylene carbonate (PC)/ EC (1:1 in volume) with 5 vol% FEC was used as the electrolyte. Galvanostatic charge-discharge were measured by a battery test system (CT2001A, LAND) with cutoff potentials from 0.01 V to 3.0 V. Cyclic voltammograms (CV) were obtained using an electrochemical workstation (Gamry Interface 1000) in the voltage range of 0–3.0 V at scan rates from 0.1 mV s^{-1} to 1 mV s^{-1}.

RESULTS AND DISCUSSION

Ni_xSn NPs with tuned composition (0.6<x<1.9) were prepared by the co-reduction of proper amounts of nickel(II) acetylacetonate and tin(II) acetate at 180 ºC by TBAB and in the presence of OAm and OAc (see experimental section for details). Following this procedure, quasi-spherical NPs with sizes in the range from 3.9 ± 0.7 nm to 4.6 ± 0.6 nm were produced (Figure 1). SEM-EDS analysis showed the Ni/Sn ratio of the Ni_xSn NPs to be 0.6, 0.9, 1.2 and 1.9 ± 0.1 for nominal Ni/Sn ratios of 0.75, 1.0, 1.5 and 2.0, respectively (Figure S1). As examples, the Ni composition of $Ni_{0.9}Sn$ and $Ni_{1.2}Sn$ by EDS were found to be 0.95 and 1.17 using ICP technology. XRD analysis displayed the crystallographic phase of all the alloys to resemble that of Sn or orthorhombic Ni_3Sn_2 (Figure 1c). Main XRD peaks did not significantly shift with the introduction of different amounts of Ni. However, as the Ni amount increased, the material crystallinity decreased and additional peaks became visible, denoting the formation of a more complex crystal phase, which did not match well with any of the reported intermetallic Ni-Sn phases.

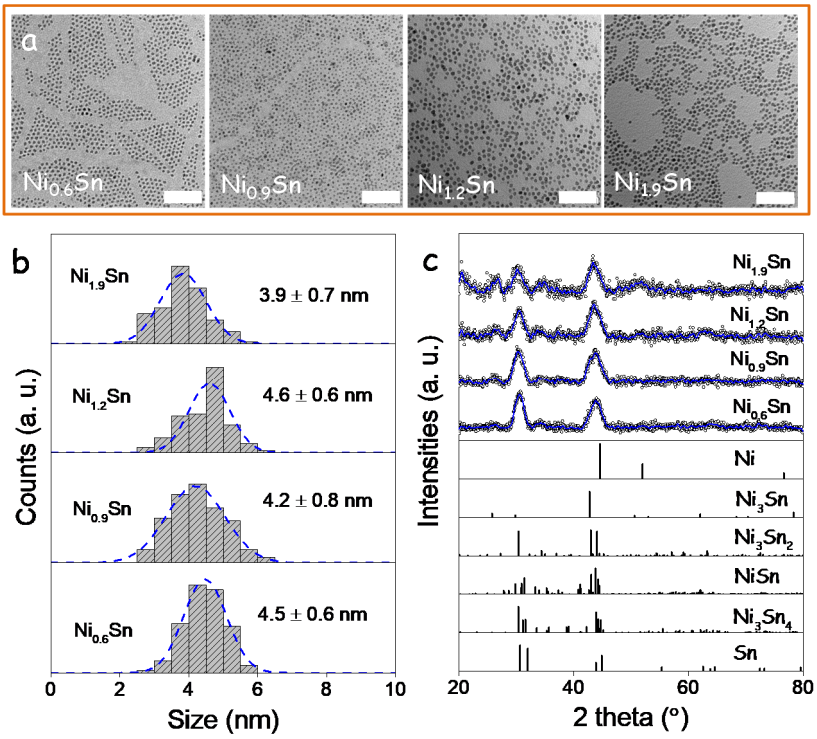

Figure 1. a) TEM micrographs of Ni-Sn NPs with different compositions, as obtained from EDX and displayed in each image. Scale bar: 50 nm. b) Size distribution histograms of the Ni-Sn NPs; c) XRD patterns of the Ni-Sn NPs with different compositions. Sn, Ni and different Ni-Sn intermetallic XRD patterns are displayed as reference.

EELS chemical composition maps showed Ni and Sn to be present in all the NPs with similar ratio (Figure 2). Additionally, uniform distributions of Ni and Sn within each NP were observed (Figure 2a). HRTEM analysis revealed the NPs to have a good crystallinity with a crystallographic phase in agreement with the Ni_3Sn_2 orthorhombic phase (space group = Pnma) with a = 7.1100 Å, b = 5.2100 Å

and c = 8.2300 Å (Figure 2b). [59] Additional EELS and HRETM for Ni1.9Sn and Ni1.2Sn was presented in Figure S2, displaying a Ni_3Sn_2 structure.

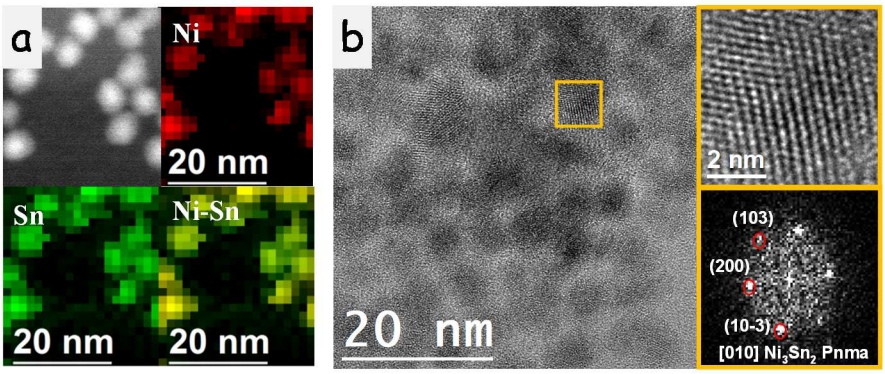

Figure 2. a) STEM and EELS compositional maps of $Ni_{0.6}Sn$ NPs. b) HRTEM micrograph of $Ni_{0.6}Sn$ NPs exposed to atmosphere and displaying a core-shell type structure. The Ni_3Sn_2 lattice fringe distances were measured to be 0.260 nm, 0.337 nm and 0.269 nm, at 69.40 and 134.54º which could be interpreted as the orthorhombic Ni_3Sn_2 phase, visualized along its [010] zone axis.

As displayed in Figures 3 and S2, XPS analysis of the Ni_xSn NPs showed Ni to be present in two different chemical states, which we associated with metallic Ni^0 (Ni $2p_{3/2}$ at 852.3 eV) and $Ni^{2+/3+}$ oxidation states (Ni $2p_{3/2}$ at 855.6 eV).[60] The ratio of the two components was found to be $Ni^{2+/3+}/Ni^0$ = 2.5. Sn was also present in two chemical states, displaying a metallic (Sn $3d_{5/2}$ peak at 484.4 eV) and an oxidized component (Sn $3d_{5/2}$ peak at 486.2 eV) with a relative ratio $Sn^{2+/4+}/Sn^0$ = 3.2.[60] We associated the oxidized states to the presence of an oxide layer at the Ni_xSn NPs surface, which had been grown during their manipulation and transportation in ambient conditions. The ratio of the two metals in $Ni_{1.2}Sn$ NPs, as measured by XPS, was Ni/Sn = 0.46, which pointed at a slight segregation of Sn to the NP surface, also consistent with the higher relative oxidized component in Sn than Ni. The XPS for other compositions were studied and presented in Figure S4, an oxidized layer was seen each. We hypothesize that this surface segregation could have taken place during oxidation.[57,61,62]

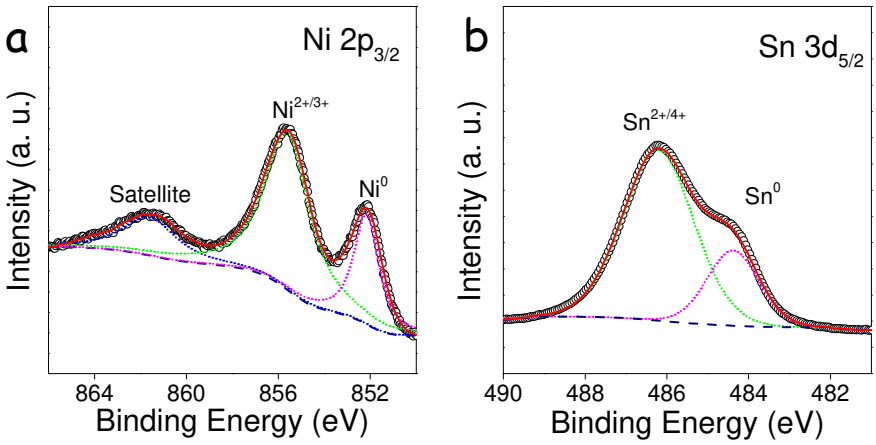

Figure 3. XPS spectra of the Ni $2P_{3/2}$ region (a) and the Sn $3d_{5/2}$ region (b) of $Ni_{1.2}Sn$ NPs.

Before testing the performance of Ni_xSn NPs as anode material in LIBs and SIBs, the organic ligands present at their surface were removed though a treatment with a mixture of hydrazine and acetonitrile. FTIR analysis confirmed the effectivity of this treatment through the disappearance of peaks at 2890 cm^{-1} and 2822 cm^{-1} that correspond to C-H stretching modes (Figure S5).[63]

To evaluate the performance of Ni_xSn NPs as anode material in LIBs and SIBs, coin-type half-cells with metallic Li or Na foil as counter electrodes were assembled. Working electrodes were prepared by mixing Ni_xSn NPs with Super P, PVDF and NMP, and coating the resulting slurry onto Cu foil. Standard liquid electrolyte formulations were used: $LiPF_6$ in EC/DEC with FEC for LIBs and $NaClO_4$ in PC/EC with FEC for SIBs.

Figure 4 shows representative initial CV profiles of the $Ni_{0.9}Sn$ NP-based electrode obtained at 0.1 mV s^{-1} in the applied potential region of 0-3.0 V vs. Li^+/Li and Na^+/Na, respectively. Significant differences were obtained between the 1st and following cycles, associated to the formation of the solid electrolyte interface (SEI) layer in both systems.[17]

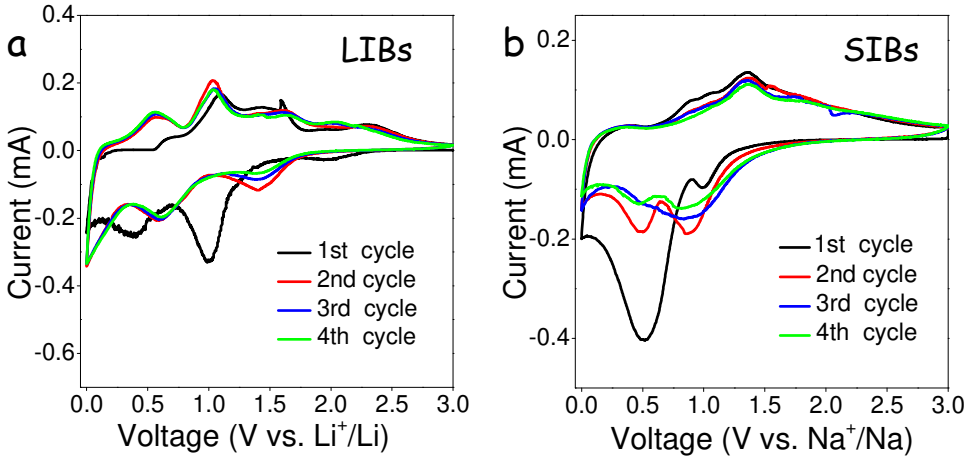

Figure 4. Initial CV curves obtained from the $Ni_{0.9}Sn$ NP-based electrode at 0.1 mV s^{-1} in the voltage window 0-3.0 V *vs.* (a) Li^+/Li (b) Na^+/Na.

Lithium reversibly interacts with Sn with a theoretical capacity of 992 mAh g^{-1}, corresponding to the alloying reaction: $Sn \rightarrow Li_{4.4}Sn$.[34] Lithium does not react with Ni. Thus, assuming no capacity contribution from Ni, the theoretical specific capacity of $Ni_{0.6}Sn$, $Ni_{0.9}Sn$, $Ni_{1.2}Sn$ and $Ni_{1.9}Sn$ electrodes was 765 mAh g^{-1}, 687 mAh g^{-1}, 623 mAh g^{-1}, and 511 mAh g^{-1}, respectively.

The cycling performance of Ni_xSn NP-based electrodes was measured by galvanostatic charging-discharging at 0.2 A g^{-1}, as shown in Figures 5 and S4. Ni_xSn NP-based electrodes delivered very large initial capacities, over 1200 mAh g^{-1}, well above their theoretical maximum. These large values were ascribed to the decomposition of the electrolyte to form the SEI layer. However, in the first few cycles, a strong capacity loss in the form of a decreased current density was observed due to the formed SEI layer. Upon continuous cycling, the charge-discharge capability decreased during dozens

of cycles, but recovered after some additional cycles up to values well above their theoretical maximum capacity, e.g. 980 mAh g^{-1} after 340 cycles for the $Ni_{0.9}Sn$ electrode (Figure 5b). On the other hand, the columbic efficiency was stabilized at ca. 99% after the first 10 cycles. Besides the SEI formation in the first few cycles, the phenomenon of a capacity decrease in the initial fifty cycles followed by an increase during subsequent cycling may be attributed to structural and compositional changes of the electrode material, resulting in a complex evolution of the electrical conductivity, the electrode porous volume and its surface area.[64] During cycling, a redistribution of Ni and Sn, and changes in the shape and size of the material domains take place, strongly influencing the electrical properties of the electrode, the amount of solid/electrolyte interphase accesible, the amount of material contributing to the storage capacity through ion diffusion and the amount of surface providing a pseudocapacitance contribution. Additionally, a capacity increase during repeated cycles is a common feature of Ni_xSn and other M_xSn (M = transition metal) alloys, which has been associated to the formation and dissolution of gel-like polymeric species in the SEI layer aided by the catalytic activity of the anode material.[65–67] Within this complex system, while the maximum theoretical capacity decreases with the amount of Ni introduced, $Ni_{0.9}Sn$ showed the highest capacity after several hundreds of cycles (Figure S6) among the different Ni_xSn compositions tested in the present work. The extra-capacity of Ni_xSn alloys, compared with their theoretical maximum, should be attributed to the ultra-small particle size and the related high surface area, which provided additional active sites for Li-ion storage that translated into an increased pseudocapacitive contribution. The relative stable cycling performance and high capacity retention could be also ascribed to the ultra-small particle size and the presence of Ni as a conductive buffer substrate, both parameters moderating the variation of stress during the alloying/dealloying process.

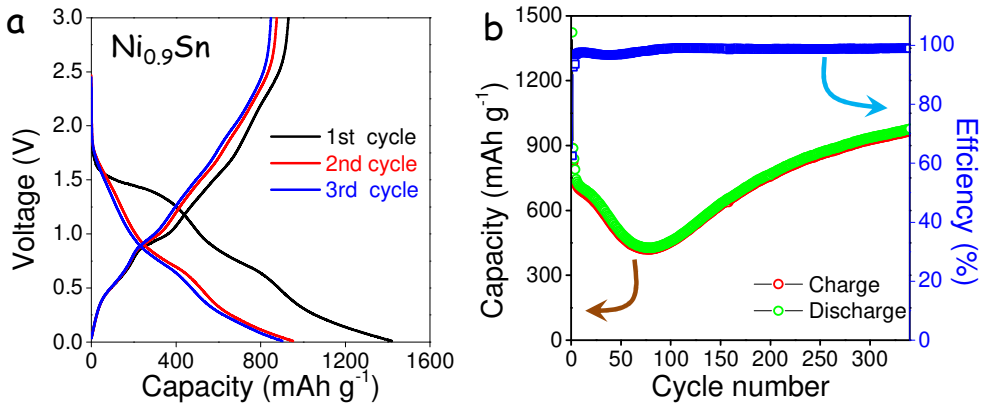

Figure 5. a) First three charge-discharge curves at 0.2 A g^{-1} for the $Ni_{0.9}Sn$ electrode. b) Charge-discharge capacity and related columbic efficiency over 340 cycles at a current density of 0.2 A g^{-1}.

To further evaluate the rate capability of the $Ni_{0.9}Sn$ NP-based electrodes, galvanostatic measurements were carried out at different current densities, between 0.1 and 2.0 A g^{-1} (Figure 6). $Ni_{0.9}Sn$ NP-based electrodes delivered average discharge capacities of 835, 702, 523, 378 and 261 mAh g^{-1} at 0.1, 0.2,

0.5, 1.0, 2.0 A g^{-1}, respectively. The notable rate capability of Ni_xSn-based electrodes was associated with their ultra-small particles size with high surface area shorting Li-ion diffusion paths and providing more channels for Li^+/electrons transporting. The inactive Ni as conductive part improved the electrical conductivity of the all Ni_xSn alloys also facilitating the diffusion of Li^+/electrons.

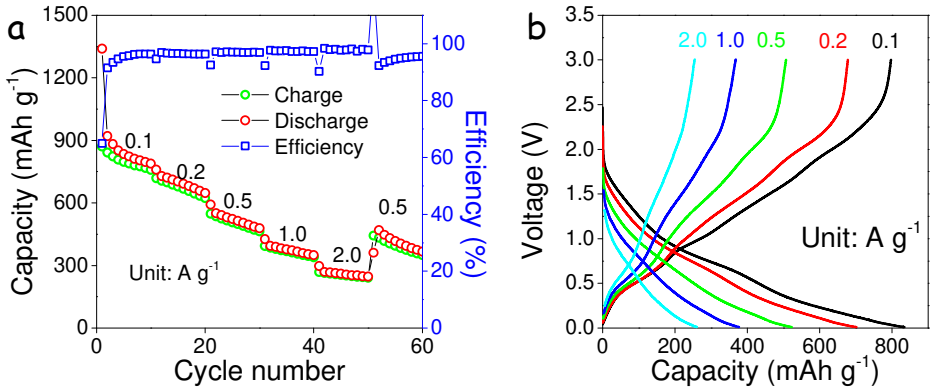

Figure 6. Li-ion storage performance of the $Ni_{0.9}Sn$ electrode: a) Rate performance at 0.1, 0.2, 0.5, 1.0, 2.0 A g^{-1}. b) Charge-discharge curves at rates: 0.1, 0.2, 0.5, 1.0, 2.0, 0.5 A g^{-1}.

The kinetics of $Ni_{0.9}Sn$ NP-based electrodes in LIBs was investigated by collecting CV curves at different scan rates: 0.1, 0.2, 0.4, 0.7, 1.0 mV s^{-1} in the potential range of 0-3.0 V vs. Li^+/Li (Figure 7a). The anodic peaks at 0.62 V and 1.04 V, and the cathodic peak at 0.54 V were observed to increase with scan rate. Generally, a potential relationship between the measured current (i) and the scan rate (ν) can be considered: [64–66]

$$i = av^b$$

According to previous reports, an ideal capacitive behavior is characterized by b = 1. On the other hand, when b is close to 0.5 the capacity is dominated by the diffusion process.[65–67] From our experimental results, the b values of the current peaks at 0.62, 0.54, 1.04 V were calculated to be 0.83, 0.66 and 0.63, respectively. All calculated b values above 0.5 indicated the $Ni_{0.9}Sn$ NP-based electrodes to be characterized by a significant pseudocapacitive contribution (Figure 7b).

At a certain potential, the current density at each scan rate can be divided into two parts, a diffusion-controlled ($k_1v^{1/2}$) fraction associated to the Li^+ insertion and a capacitor-like fraction (k_2v) :[65–67]

$$i(V) = k_1v^{1/2} + k_2v$$

Thus, k_1 and k_2 can be determined by plotting $i(V)/v^{1/2}$ vs. $v^{1/2}$, distinguishing in this way the two contributions. Figure 7c shows a CV at 0.4 mV s^{-1} where the two components have been differentiated: the capacitive current as the blue shaded region and the diffusion component in red. Similarly, the two contributions are differentiated in the CVs at 0.1, 0.2, 0.7 and 1.0 mV s^{-1} in Figure S7. All these data are summarized in Figure 7d. Overall, increasing capacitive contributions were obtained when

increasing the scan rate, reaching a capacitive contribution up to 72% at 1.0 mV s^{-1}. This increased contribution with the scan rate is related to the slower Li^+ diffusion that translates into minor Li^+ in-depth alloying when compared with the faster and less rate-depended contribution of the surface reaction. High capacitive contributions, such as the ones found for Ni_xSn alloys, are highly beneficial because surface processes are much faster and stable than diffusion-controlled alloying. The high capacitive contributions also illuminated the origin of the notable rate capability of $Ni_{0.9}Sn$ NP-based electrodes. We also conducted the kinetic analysis of the Li-ion storage performance of other NiSn electrodes. As shown in Figure S8. At the same scanning rate, similar capacitive contribution were obtained for the Ni_xSn ($1.9 \leqslant x \leqslant 0.9$), larger than that of $Ni_{0.6}Sn$. By comparing the capacity and durability performance of the Ni_xSn electrode, it is rather rigorous not to draw a conclusion that it is relevant to the pseudocapacitive process.

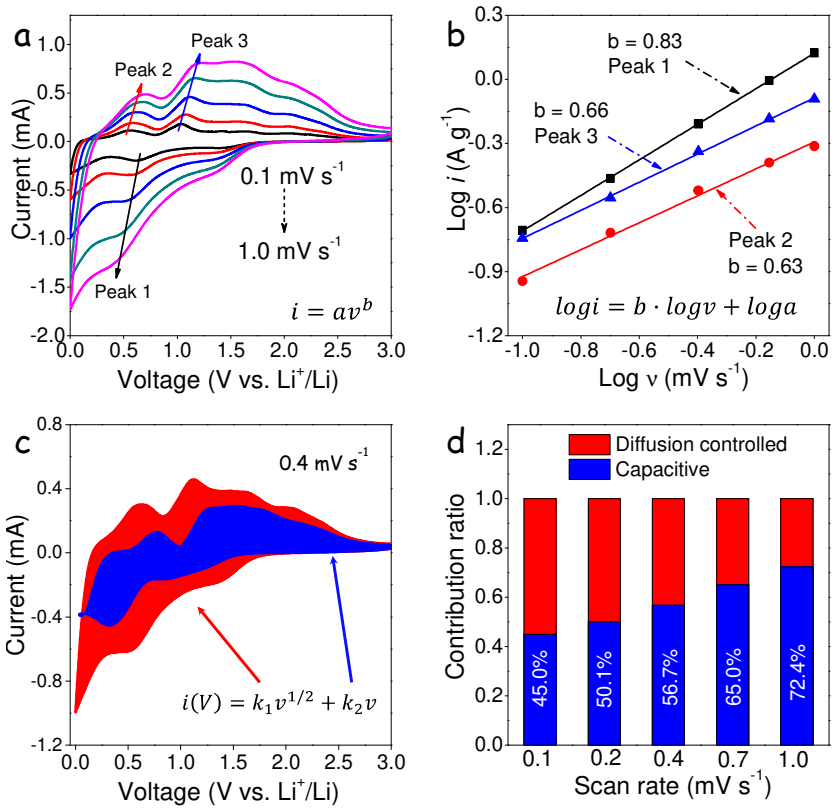

Figure 7. Kinetic analysis of the Li-ion storage performance of the $Ni_{0.9}Sn$ electrode: a) CV curves at the scan rates of 0.1, 0.2, 0.4, 0.7, 1.0 mV s^{-1}. b) Logarithmic dependence between peak current density and scan rate at the peaks 0.62, 0.54 and 1.04 V. c) Capacitive contribution (blue region) to the total current contribution at 0.4 mV s^{-1}. d) Normalized contribution ratio of capacitive part and diffusion-controlled fraction at the scan rates of 0.1, 0.2, 0.4, 0.7, 1.0 mV s^{-1}.

Sodium is also reversibly stored in Sn, with a maximum theoretical capacity of 847 mAh g^{-1} corresponding to the reaction: $Sn \rightarrow Na_{3.75}Sn$.[17] Considering that Ni does not contribute to any Na-ion capacity, thus the theoretical capacity of $Ni_{0.6}Sn$, $Ni_{0.9}Sn$, $Ni_{1.2}Sn$ and $Ni_{1.9}Sn$ electrodes is 653 mAh g^{-1}, 586 mAh g^{-1}, 532 mAh g^{-1}, and 437 mAh g^{-1}, respectively.

Figures 8 and S9 present the Na-ion storage performance of Ni_xSn NP-based electrodes over 120 cycles at 0.1 A g^{-1}. Again, while capacity should decrease with the Ni content, $Ni_{0.9}Sn$ NPs exhibited the highest capacities among the different compositions tested. In the first cycles, Na-ion discharge-charge storage capacities above 300 mAh g^{-1} at 0.1 A g^{-1} were obtained for the $Ni_{0.9}Sn$ NP-based electrode. However, upon subsequent cycling, a monotonous capacity decrease was observed, decaying to 160 mAh g^{-1} at the 120th cycle. It is worth noting that the smaller Na-ion storage capacity, when compared with Li-ion, is ascribed to the larger radius of Na^+ than Li^+, causing less Na^+ in-depth alloying. Rate-capability tests in the window 0.1-2.0 A g^{-1} showed the $Ni_{0.9}Sn$ NP-based electrode to deliver average discharge capacities of 327, 258, 217, 168, 128, and 88 mAh g^{-1} at 0.05, 0.1, 0.2, 0.5, 1.0, and 2.0 A g^{-1}, respectively. In addition, $Ni_{0.9}Sn$ NP-based electrodes showed similar capacities at 0.1 and 0.2 A g^{-1} after 30-40 more cycles at higher discharging-charging rate (Figure 8d).

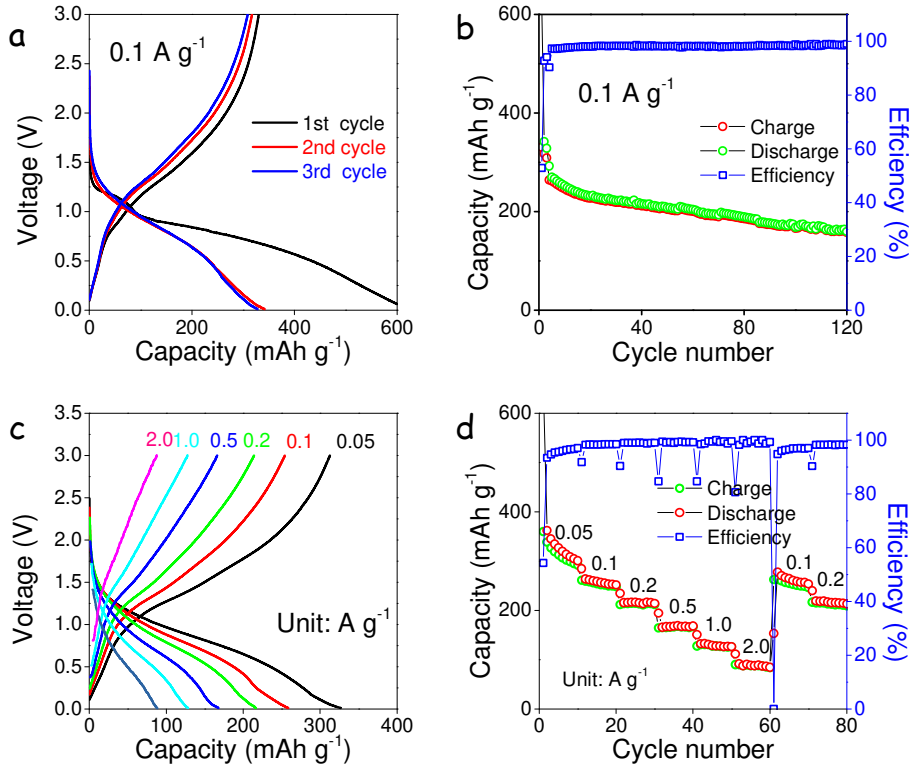

Figure 8. Na-ion storage performance of the $Ni_{0.9}Sn$ electrode: a) Typical first three charging-discharging curves at 0.1 A g^{-1}. b) Charge-discharge capacity and related efficiency over 120 cycles at a current density of 0.1 A g^{-1}. c) Selected charging-discharging curves at 0.05, 0.1, 0.2, 0.5, 1.0, 2.0, 0.1 and 0.2 A g^{-1} rates. d) Rate capabilities of $Ni_{0.9}Sn$ at 0.05, 0.1, 0.2, 0.5, 1.0 and 2.0 A g^{-1}.

The kinetics of $Ni_{0.9}Sn$ NP-based electrodes in SIBs was investigated in a similar way as in LIBs, by collecting CV curves at different scan rates: 0.1, 0.2, 0.4, 0.7, 1.0 mV s^{-1}. $Ni_{0.9}Sn$ NP-based electrodes in SIBs were characterized with b values of 0.91 and 0.84 at 0.85 V and 1.36 V, respectively. Higher b values already pointed out at a relatively higher capacitance contribution in SIBs than LIBs. This phenomenon could be associated with the larger radius of Na^+, which increased the diffusion resistance into the interior of the materials and caused a larger fraction of Na^+ to exist on the surface,

leading to higher capacitive contributions in SIBs than in LIBs. As shown in Figures S8 and 9, contributions up to 84% at 1.0 mV s^{-1} were measured from $Ni_{0.9}Sn$ NP-based electrodes in SIBs.

$Ni_{0.9}Sn$ was selected as an example to conduct the EIS study in Li- and Na-ion batteries, as shown in Figure S10, revealing that the NiSn provides small charge-transfer resistances.

CONCLUSION

In summary, we reported the synthesis of Ni_xSn NPs with tuned composition ($0.6 \leq x \leq 1.9$) and their performance as anode material in LIBs and SIBs. Among the different compositions tested, best performances toward Li^+ ion and Na^+ ion insertion were obtained for $Ni_{0.9}Sn$ NP-based electrodes. This optimized cycling charge-discharge performance for LIBs provided 980 mAh g^{-1} at 0.2 A g^{-1} after 340 cycles. Additionally, $Ni_{0.9}Sn$ NP-based electrodes were tested in Na^+-ion half cells, exhibiting 160 mAh g^{-1} over 120 cycles at 0.1 A g^{-1}. From CV measurements at different current rates, it was found that the charging process was both capacitive and diffusion controlled, while the capacitive contribution was dominant in both LIBs and SIBs. The pseudocapacitive charge-storage accounted for a high portion of the whole energy storage capacity, which was associated to the small size and the composition of the Ni_xSn NPs used.

Author Information

○ J. Li and X. Xu equally contributed to this work.

Corresponding Author

* Andreu Cabot: acabot@irec.cat

* Jun Liu: msjliu@scut.edu.cn

Author contribution

The manuscript was prepared through the contribution of all authors. A. Cabot and J. Liu conceived and guided the project, and supervised the work. J. Li designed the experiments, produced the NPs, conducted XRD, TEM, SEM-EDS and FT-IR characterization, and wrote the first draft of the manuscript. X. Xu performed the electrochemical measurements. Z. Luo, C. Zhang, X. Yu and Y. Zuo significantly contributed to the results discussion. T. Zhang, P. Tang, and J. Arbiol performed structural and compositional NCs characterization by means of HRTEM and EELS, and discussed the results. J. Llorca measured and discussed XPS data. The manuscript was corrected and improved by all authors.

ACKNOWLEDGMENTS

This work was supported by the European Regional Development Funds and by the Spanish Ministerio de Economía y Competitividad through the project SEHTOP (ENE2016-77798-C4-3-R). J. Li thanks the China Scholarship Council for scholarship support. This project was supported by the National Natural Science Foundation of China (no. 51771076), the "1000 plan" from Chinese Government, and the Project of Public Interest Research and Capacity Building of Guangdong Province (no. 2017A010104004). T. Zhang, P. Tang and J. Arbiol acknowledge funding from Generalitat de Catalunya 2017 SGR 327 and the Spanish MINECO coordinated projects between IREC and ICN2 VALPEC and subprojects RESOL and ANAPHASE (ENE2017-85087-C3). ICN2 acknowledges support from the Severo Ochoa Programme (MINECO, Grant no. SEV-2013-0295) and is funded by the CERCA Programme / Generalitat de Catalunya. T. Zhang has received funding from the CSC-UAB PhD scholarship program. Part of the present work has been performed in the framework of Universitat Autònoma de Barcelona Materials Science PhD program. J. Llorca is a Serra Húnter Fellow and is grateful to ICREA Academia program and to MINECO/FEDER grant ENE2015-63969-R and GC 2017 SGR 128.

Conflict of interest

The authors declare no competing financial interest.

Supporting Information

Supplementary material related to this article can be found.

References

[1] C.M. Park, J.H. Kim, H. Kim, H.J. Sohn, Li-alloy based anode materials for Li secondary batteries, Chem. Soc. Rev. 39 (2010) 3115–3141.

[2] D. Larcher, J.M. Tarascon, Towards greener and more sustainable batteries for electrical energy storage, Nat. Chem. 7 (2015) 19–29.

[3] J.B. Goodenough, K.S. Park, The Li-ion rechargeable battery: A perspective, J. Am. Chem. Soc. 135 (2013) 1167–1176.

[4] M.D. Slater, D. Kim, E. Lee, C.S. Johnson, Sodium-ion batteries, Adv. Funct. Mater. 23 (2013) 947–958.

[5] M.R. Palacín, Recent advances in rechargeable battery materials: A chemist's perspective, Chem. Soc. Rev. 38 (2009) 2565–2575.

[6] X. Liu, J. Zhang, W. Si, L. Xi, B. Eichler, C. Yan, O.G. Schmidt, Sandwich Nanoarchitecture of Si/Reduced Graphene Oxide Bilayer Nanomembranes for Li-Ion Batteries with Long Cycle Life, ACS Nano. 9 (2015) 1198–1205.

[7] C. Yan, W. Xi, W. Si, J. Deng, O.G. Schmidt, Highly Conductive and Strain-Released Hybrid Multilayer Ge/Ti Nanomembranes with Enhanced Lithium-Ion-Storage Capability, Adv. Mater. 25 (2013) 539–544.

[8] Y. Wen, K. He, Y. Zhu, F. Han, Y. Xu, I. Matsuda, Y. Ishii, J. Cumings, C. Wang, Expanded graphite as superior anode for sodium-ion batteries, Nat. Commun. 5 (2014) 4033.

[9] M.F. Oszajca, M.I. Bodnarchuk, M. V. Kovalenko, Precisely engineered colloidal nanoparticles and nanocrystals for Li-ion and Na-ion batteries: Model systems or practical solutions?, Chem. Mater. 26 (2014) 5422–5432.

[10] N. Liu, Z. Lu, J. Zhao, M.T. Mcdowell, H.W. Lee, W. Zhao, Y. Cui, A pomegranate-inspired nanoscale design for large-volume-change lithium battery anodes, Nat. Nanotechnol. 9 (2014) 187–192.

[11] J. Deng, H. Ji, C. Yan, J. Zhang, W. Si, S. Baunack, S. Oswald, Y. Mei, O.G. Schmidt, Naturally Rolled-Up C/Si/C Trilayer Nanomembranes as Stable Anodes for Lithium-Ion Batteries with Remarkable Cycling Performance, Angew. Chemie Int. Ed. 52 (2013) 2326–

2330.

[12] F. Nacimiento, P. Lavela, J.L. Tirado, J.M. Jiménez-Mateos, A facile carbothermal preparation of Sn-Co-C composite electrodes for Li-ion batteries using low-cost carbons, J. Solid State Electrochem. 16 (2012) 953–962.

[13] J.-Y. Hwang, S.-T. Myung, Y.-K. Sun, Sodium-ion batteries: present and future, Chem. Soc. Rev. 46 (2017) 3529–3614.

[14] M. Lao, Y. Zhang, W. Luo, Q. Yan, W. Sun, S.X. Dou, Alloy-Based Anode Materials toward Advanced Sodium-Ion Batteries, Adv. Mater. 29 (2017).

[15] P.G. Bruce, B. Scrosati, J.M. Tarascon, Nanomaterials for rechargeable lithium batteries, Angew. Chemie - Int. Ed. 47 (2008) 2930–2946.

[16] H. Tian, F. Xin, X. Wang, W. He, W. Han, High capacity group-IV elements (Si, Ge, Sn) based anodes for lithium-ion batteries, J. Mater. 1 (2015) 153–169.

[17] J. Liu, Y. Wen, P.A. Van Aken, J. Maier, Y. Yu, Facile synthesis of highly porous Ni-Sn intermetallic microcages with excellent electrochemical performance for lithium and sodium storage, Nano Lett. 14 (2014) 6387–6392.

[18] R. Marom, S.F. Amalraj, N. Leifer, D. Jacob, D. Aurbach, A review of advanced and practical lithium battery materials, J. Mater. Chem. 21 (2011) 9938–9954.

[19] J. Wen, Y. Yu, C. Chen, A Review on Lithium-Ion Batteries Safety Issues: Existing Problems and Possible Solutions, Mater. Express. 2 (2012) 197–212.

[20] B. Wang, B. Luo, X. Li, L. Zhi, The dimensionality of Sn anodes in Li-ion batteries, Mater. Today. 15 (2012) 544–552.

[21] C. Vaalma, D. Buchholz, M. Weil, S. Passerini, A cost and resource analysis of sodium-ion batteries, Nat. Rev. Mater. 3 (2018) 18013.

[22] M.N. Obrovac, V.L. Chevrier, Alloy negative electrodes for Li-ion batteries, Chem. Rev. 114 (2014) 11444–11502.

[23] N. Nitta, F. Wu, J.T. Lee, G. Yushin, Li-ion battery materials: Present and future, Mater. Today. 18 (2015) 252–264.

[24] A.R. Kamali, D.J. Fray, Tin-based materials as advanced anode materials for lithium ion batteries: A review, Rev. Adv. Mater. Sci. 27 (2011) 14–24.

[25] M. Walter, S. Doswald, F. Krumeich, M. He, R. Widmer, N.P. Stadie, M. V. Kovalenko,

Oxidized Co-Sn nanoparticles as long-lasting anode materials for lithium-ion batteries, Nanoscale. 10 (2018) 3777–3783.

[26] M.F. Oszajca, M.I. Bodnarchuk, M. V. Kovalenko, Precisely engineered colloidal nanoparticles and nanocrystals for Li-ion and Na-ion batteries: Model systems or practical solutions?, Chem. Mater. 26 (2014) 5422–5432.

[27] K. Kravchyk, L. Protesescu, M.I. Bodnarchuk, F. Krumeich, M. Yarema, M. Walter, C. Guntlin, M. V. Kovalenko, Monodisperse and inorganically capped Sn and Sn/SnO2nanocrystals for high-performance Li-ion battery anodes, J. Am. Chem. Soc. 135 (2013) 4199–4202.

[28] M. He, M. Walter, K. V. Kravchyk, R. Erni, R. Widmer, M. V. Kovalenko, Monodisperse SnSb nanocrystals for Li-ion and Na-ion battery anodes: Synergy and dissonance between Sn and Sb, Nanoscale. 7 (2015) 455–459.

[29] C. Chen, Y. Wen, X. Hu, X. Ji, M. Yan, L. Mai, P. Hu, B. Shan, Y. Huang, Na^+ intercalation pseudocapacitance in graphene-coupled titanium oxide enabling ultra-fast sodium storage and long-term cycling, Nat. Commun. 6 (2015) 6929.

[30] T. Brezesinski, J. Wang, S.H. Tolbert, B. Dunn, Ordered mesoporous α-MoO3with iso-oriented nanocrystalline walls for thin-film pseudocapacitors, Nat. Mater. 9 (2010) 146–151.

[31] W.X. Lei, Y. Pan, Y.C. Zhou, W. Zhou, M.L. Peng, Z.S. Ma, CNTs-Cu composite layer enhanced Sn-Cu alloy as high performance anode materials for lithium-ion batteries, RSC Adv. 4 (2014) 3233–3237.

[32] Y.M. Lin, P.R. Abel, A. Gupta, J.B. Goodenough, A. Heller, C.B. Mullins, Sn-Cu nanocomposite anodes for rechargeable sodium-ion batteries, ACS Appl. Mater. Interfaces. 5 (2013) 8273–8277.

[33] X.L. Wang, W.Q. Han, J. Chen, J. Graetz, Single-crystal intermetallic M-Sn (M = Fe, Cu, Co, Ni) nanospheres as negative electrodes for lithium-ion batteries, ACS Appl. Mater. Interfaces. 2 (2010) 1548–1551.

[34] S. Wang, M. He, M. Walter, F. Krumeich, K. V. Kravchyk, M. V. Kovalenko, Monodisperse $CoSn_2$ and $FeSn_2$ nanocrystals as high-performance anode materials for lithium-ion batteries, Nanoscale. 10 (2018) 6827–6831.

[35] L.O. Vogt, C. Villevieille, Elucidation of the reaction mechanisms of isostructural $FeSn_2$ and $CoSn_2$ negative electrodes for Na-ion batteries, J. Mater. Chem. A. 5 (2017) 3865–3874.

[36] N. Tamura, Y. Kato, A. Mikami, M. Kamino, S. Matsuta, S. Fujitani, Study on Sn–Co Alloy Anodes for Lithium Secondary Batteries, J. Electrochem. Soc. 153 (2006) A1626.

[37] Z. Du, S. Zhang, Enhanced electrochemical performance of Sn-Co nanoarchitectured electrode for lithium ion batteries, J. Phys. Chem. C. 115 (2011) 23603–23609.

[38] C.M. Ionica-Bousquet, P.E. Lippens, L. Aldon, J. Olivier-Fourcade, J.C. Jumas, In situ 119 Sn Mössbauer Effect Study of Li−CoSn 2 Electrochemical System, Chem. Mater. 18 (2006) 6442–6447.

[39] J. Zhu, D. Wang, T. Liu, C. Guo, Preparation of Sn-Co-graphene composites with superior lithium storage capability, Electrochim. Acta. 125 (2014) 347–353.

[40] X. Shi, H. Song, A. Li, X. Chen, J. Zhou, Z. Ma, Sn-Co nanoalloys embedded in porous N-doped carbon microboxes as a stable anode material for lithium-ion batteries, J. Mater. Chem. A. 5 (2017) 5873–5879.

[41] G.O. Park, J. Yoon, J.K. Shon, Y.S. Choi, J.G. Won, S. Bin Park, K.H. Kim, H. Kim, W.S. Yoon, J.M. Kim, Discovering a Dual-Buffer Effect for Lithium Storage: Durable Nanostructured Ordered Mesoporous Co-Sn Intermetallic Electrodes, Adv. Funct. Mater. 26 (2016) 2800–2808.

[42] B.O. Jang, S.H. Park, W.J. Lee, Electrospun Co-Sn alloy/carbon nanofibers composite anode for lithium A ion batteries, J. Alloys Compd. 574 (2013) 325–330.

[43] X. Liu, J. Xie, H. Zhao, P. Lv, K. Wang, Z. Feng, K. ̄wierczek, Electrochemical properties of mechanochemically synthesized CoSn2-C nanocomposite-type anode material for Li-ion batteries, Solid State Ionics. 269 (2015) 86–92.

[44] J.R. González, F. Nacimiento, R. Alcántara, G.F. Ortiz, J.L. Tirado, Electrodeposited CoSn2 on nickel open-cell foam: Advancing towards high power lithium ion and sodium ion batteries, CrystEngComm. 15 (2013) 9196–9202.

[45] R. Gnanamuthu, Y.N. Jo, C.W. Lee, Brush electroplated CoSn2alloy film for application in lithium-ion batteries, J. Alloys Compd. 564 (2013) 95–99.

[46] G. Ferrara, C. Arbizzani, L. Damen, M. Guidotti, M. Lazzari, F.G. Vergottini, R. Inguanta, S. Piazza, C. Sunseri, M. Mastragostino, High-performing Sn-Co nanowire electrodes as anodes for lithium-ion batteries, J. Power Sources. 211 (2012) 103–107.

[47] P.P. Ferguson, A.D.W. Todd, J.R. Dahn, Comparison of mechanically alloyed and sputtered tin-cobalt-carbon as an anode material for lithium-ion batteries, Electrochem. Commun. 10

(2008) 25–31.

[48] J. He, H. Zhao, J. Wang, J. Wang, J. Chen, Hydrothermal synthesis and electrochemical properties of nano-sized Co-Sn alloy anodes for lithium ion batteries, J. Alloys Compd. 508 (2010) 629–635.

[49] S. Il Lee, S. Yoon, C.M. Park, J.M. Lee, H. Kim, D. Im, S.G. Doo, H.J. Sohn, Reaction mechanism and electrochemical characterization of a Sn-Co-C composite anode for Li-ion batteries, Electrochim. Acta. 54 (2008) 364–369.

[50] P. Chen, L. Guo, Y. Wang, Graphene wrapped SnCo nanoparticles for high-capacity lithium ion storage, J. Power Sources. 222 (2013) 526–532.

[51] J. Shin, W.-H. Ryu, K.-S. Park, I.-D. Kim, Morphological evolution of carbon nanofibers encapsulating SnCo alloys and its effect on growth of the solid electrolyte interphase layer, ACS Nano. 7 (2013) 7330–7341.

[52] J. Zhang, Y. Xia, Co-Sn Alloys as Negative Electrode Materials for Rechargeable Lithium Batteries, J. Electrochem. Soc. 153 (2006) A1466.

[53] N. Mahmood, C. Zhang, F. Liu, J. Zhu, Y. Hou, Hybrid of Co3Sn2@Co nanoparticles and nitrogen-doped graphene as a lithium ion battery anode, ACS Nano. 7 (2013) 10307–10318.

[54] D. wei ZHANG, C. ge YANG, J. DAI, J. wu WEN, L. WANG, C. hua CHEN, Fabrication of Sn-Ni alloy film anode for Li-ion batteries by electrochemical deposition, Trans. Nonferrous Met. Soc. China (English Ed. 19 (2009) 1489–1493.

[55] M. Uysal, T. Cetinkaya, A. Alp, H. Akbulut, Active and inactive buffering effect on the electrochemical behavior of Sn-Ni/MWCNT composite anodes prepared by pulse electrodeposition for lithium-ion batteries, J. Alloys Compd. 645 (2015) 235–242.

[56] X. Fan, P. Dou, A. Jiang, D. Ma, X. Xu, One-step electrochemical growth of a three-dimensional Sn-Ni@PEO nanotube array as a high performance lithium-ion battery anode, ACS Appl. Mater. Interfaces. 6 (2014) 22282–22288.

[57] J. Li, Z. Luo, Y. Zuo, J. Liu, T. Zhang, P. Tang, J. Arbiol, J. Llorca, A. Cabot, NiSn bimetallic nanoparticles as stable electrocatalysts for methanol oxidation reaction, Appl. Catal. B Environ. 234 (2018) 10–18.

[58] M. Walter, S. Doswald, M. V. Kovalenko, Inexpensive colloidal SnSb nanoalloys as efficient anode materials for lithium- and sodium-ion batteries, J. Mater. Chem. A. 4 (2016) 7053–7059.

[59] H. Fjellvåg, A. Kjekshus, R. Stomberg, R. Zingales, I. Vikholm, F. Urso, J. Weidlein, R.A.

Zingaro, Structural Properties of Co3Sn2, Ni3Sn2 and Some Ternary Derivatives., Acta Chem. Scand. 40a (1986) 23–30.

[60] C.D. Wager, W.M. Riggs, L.E. Davis, J.F. Moulder, G.E. Muilenderg. Handbook of X-ray photoelectron spectroscopy. 1979.

[61] Y. Liu, X. Liu, Q. Feng, D. He, L. Zhang, C. Lian, R. Shen, G. Zhao, Y. Ji, D. Wang, G. Zhou, Y. Li, Intermetallic NixMy(M = Ga and Sn) Nanocrystals: A Non-precious Metal Catalyst for Semi-Hydrogenation of Alkynes, Adv. Mater. 28 (2016) 4747–4754.

[62] M. He, L. Protesescu, R. Caputo, F. Krumeich, M. V. Kovalenko, A general synthesis strategy for monodisperse metallic and metalloid nanoparticles (In, Ga, Bi, Sb, Zn, Cu, Sn, and Their Alloys) via in situ formed metal long-chain amides, Chem. Mater. 27 (2015) 635–647.

[63] J. Li, Z. Luo, F. He, Y. Zuo, C. Zhang, J. Liu, X. Yu, R. Du, T. Zhang, M.F. Infante-Carrió, P. Tang, J. Arbiol, J. Llorca, A. Cabot, Colloidal Ni–Co–Sn nanoparticles as efficient electrocatalysts for the methanol oxidation reaction, J. Mater. Chem. A. (2018).

[64] H.-S. Kim, J.B. Cook, S.H. Tolbert, B. Dunn, The Development of Pseudocapacitive Properties in Nanosized-MoO2, J. Electrochem. Soc. 162 (2015) A5083–A5090.

[65] V. Augustyn, P. Simon, B. Dunn, Pseudocapacitive oxide materials for high-rate electrochemical energy storage, Energy Environ. Sci. 7 (2014) 1597–1614.

[66] X. Xu, S. Ji, M. Gu, J. Liu, In Situ Synthesis of MnS Hollow Microspheres on Reduced Graphene Oxide Sheets as High-Capacity and Long-Life Anodes for Li- and Na-Ion Batteries, ACS Appl. Mater. Interfaces. 7 (2015) 20957–20964.

[67] X. Xu, J. Liu, J. Liu, L. Ouyang, R. Hu, H. Wang, L. Yang, M. Zhu, A General Metal-Organic Framework (MOF)-Derived Selenidation Strategy for In Situ Carbon-Encapsulated Metal Selenides as High-Rate Anodes for Na-Ion Batteries, Adv. Funct. Mater. 28 (2018) 1707573.

TOC graphics

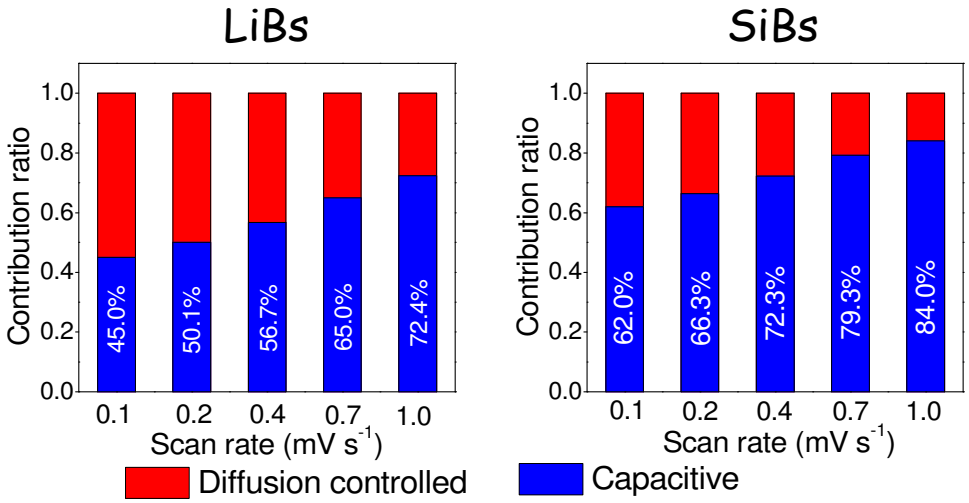

Pseudocapacitive contribution comparison between LiBs and SiBs.